Article

Measurement of Period Length and Skew Angle Patterns of Textile Cutting Pieces Based on Faster R-CNN

Lei Geng [1,2] ⬤, **Qinglei Meng** [1,2], **Zhitao Xiao** [1,2,*] **and Yanbei Liu** [1,2]

1   School of Electronics and Information Engineering, Tianjin Polytechnic University, NO.399 Binshui West Street Xiqing District, Tianjin 300387, China
2   Tianjin Key Laboratory of Optoelectronic Detection Technology and Systems, NO.399 Binshui West Street Xiqing District, Tianjin 300387, China
*   Correspondence: xiaozhitao@tjpu.edu.cn

check for updates

Abstract: The skew angle and period length of the multi-period pattern are two critical parameters for evaluating the quality of textile cutting pieces. In this paper, a new measurement method of the skew angle and period length is proposed based on Faster region convolutional neural network (R-CNN). First, a dataset containing approximately 5000 unique pattern images was established and annotated in the format of PASCAL VOC 2007. Second, the Faster R-CNN model was used to detect the pattern to determine the approximate location of the pattern (the position of the whole pattern). Third, precise position of the pattern (geometric center points of pattern) are processed based on the approximate position results using the automatic threshold segmentation method. Finally, the four-neighbor method was used to fill the missing center points to obtain a complete center point map, and the skew angle and period length can be measured by the detected center points. The experimental results show that the mean average position (mAP) of the pattern detection reached 84%, the average error of the proposed algorithm was less than 5% compared with the error of the manual measurement.

Keywords: faster R-CNN; cutting pieces; multi-period pattern; skew angle; period length

1. Introduction

Textile cutting pieces [1], as semi-finished products, have been widely used in car seats and garments areas. Most of the finished products are stitched from these pieces, and the performance of the pieces (see Figure 1a) is a key to determining the quality of the finished product. The quality of the textile pieces depends largely on their preformed geometry structure, such as the period length and skew angle of the pattern. The skew angles θ_{weft} and θ_{warp} are defined as the angle between the line along the horizontal or vertical period direction of the pattern and the overall contour of the piece (see Figure 1b). The skew angle is a critical parameter of multi-period pattern pieces, for it can affect the overall regularity of the pattern. The period length T_{hi} and T_{vi} ($i = 1, 2 \dots$) are defined as the length of one complete pattern period distance in the horizontal and vertical directions, can be used to infer the local regularity of the pattern (see Figure 1b). These two parameters can reflect the design difference between the pattern sample and the standard template, so they can be used as a criterion for judging the quality of the pattern.

(**a**)   (**b**)
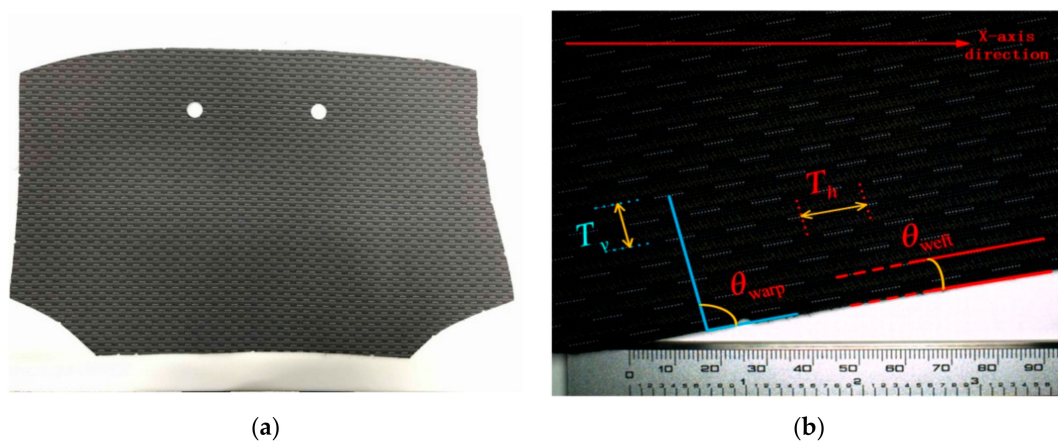
Figure 1. Textile cutting piece of car seat and pattern parameters. (**a**) The overall outline of the cutting piece with strip-shaped pattern in the global perspective. (**b**) The local part of (a) where T_h is weft period length, T_v is warp period length. θ_{weft} is weft skew angle, and θ_{warp} is warp skew angle.

The two parameters are used to check whether the cutting pieces are qualified or not in the industrial area. At present, the manual method is still the main measurement way, which is time and manpower-consuming, and due to the large amount of pattern types, only limited numbers of cutting pieces are sampled. In addition, a cutting piece with complicated patterns cannot be effectively detected by the human eyes, and this phenomenon often causes quality problems.

The periodicity of the pattern has great research significance for the pattern fabric, and is the basis for measuring the skew angle and period length of the multi-period pattern. Therefore, the period extraction of the pattern becomes the key and difficult point in measuring the parameters of a pattern. In recent years, with the rapid development of image processing technology, many approaches have been proposed for fabric periodic research. In general, these approaches can be classified into three groups: grey level co-occurrence matrix-based (GLCM) [2]; distance matching function-based (DMF) [3]; and image autocorrelation function-based [4]. The method based on GLCM is a common technique in statistical image analysis that is used to estimate image properties related to second-order statistics. Li [5] and his colleagues research the variation of the eigenvalues of four grey level co-occurrence matrices to determine the period characteristics of texture, and achieved relatively good results. Xiao, et al. [6] calculated the correlation coefficient between different regions enclosed by fabric yarns based on the grey level co-occurrence matrix method to complete the segmentation of a striped fabric. The features calculated by the co-occurrence matrix can be used for periodic detection of finite-size pattern images and the computation speed is relatively fast. However, since the quantization angle and distance are frequently used to reduce the computation time when calculating the co-occurrence matrix features, the accuracy of texture cycle extraction is significantly reduced. The method based on DMF can directly use the grey value of the texture to find the texture period and requires less computation time than the traditional co-occurrence matrix approach. Jing [7] determined the period of the printed fabrics by calculating the maximum value of the second forward difference of the two-dimensional DMF. Zhou [8] implemented an automatic measurement of the texture period of woven fabric images by combining frequency domain analysis with a distance matching function and improved the stability and computational efficiency of cycle measurement. The distance matching function is an effective method for extracting pattern period. For images of any size, the distance matching function has a faster calculation speed than the traditional co-occurrence matrix method. It is suitable for patterns of finite size. However, when the brightness and shape of the periodic pattern are inconsistent, the distance matching function cannot effectively extract the pattern period. The method based on an autocorrelation function calculates the correlation coefficient of the texture by the autocorrelation function of the image to analyze the periodicity of the texture. Wu [9] calculated the autocorrelation function of the texture edge to determine the matrix of the autocorrelation function, and

then extracted the periodic and directional features of the texture. The image autocorrelation function method is easy to implement and has strong adaptability. However, the pattern period detection method based on the autocorrelation function can only reflect the periodic features of the pattern and has no other features. Moreover, it cannot efficiently acquire periodic information of a periodic pattern that has a sparsely distributed and large size in the image. Similarly, the measurement of the surface braiding angle and pitch length of the three-dimensional braided composite was realized by the corner detection-based method [10–12]. However, this algorithm based on corner detection is not suitable for the measurement of multi-period pattern parameters. When faced with complicated patterns, the corner points detected by the corner detection algorithm are disordered and the pseudo corner points are too many, and the center point of the pattern cannot be accurately found, so that the pattern period cannot be effectively extracted.

In this paper, a new measurement method based on Faster region convolutional neural network (R-CNN) [13] was proposed to measure the parameters of the multi-period pattern. At present, Faster R-CNN has been applied in many fields, such as license plate detection [14], scene text detection [15] and optical image detection [16], and achieved excellent results with its powerful performance. As Faster R-CNN has the advantages of high object detection accuracy, fast speed and strong adaptability, we used Faster R-CNN as the pattern detector to locate the pattern and extract the pattern period. The contributions of this paper are as follows:

- We have established the first multi-period pattern dataset. This dataset contains 5000 pattern images with size of 512×640 pixels and contains a total of six types of patterns. Moreover, each pattern in the image was annotated as an object in VOC 2007 format.
- We have proposed to use the object detection network in deep learning to locate the pattern. We selected the training model of Faster R-CNN as the pattern detector and generated the bounding boxes enclosing the patterns to achieve the approximate positioning of the pattern.
- We have proposed an automatic threshold method to extract the contour of the pattern and calculated the center points to obtain the precise positioning of the pattern. The four-neighbor-method was used to fill the missing center points to acquire the center point map that reflects the periodic characteristics of the pattern.

2. Methods

In this section, the period length and pattern skew angles of textile cutting pieces were measured based on Faster R-CNN. Firstly, original images were acquired and the pattern dataset were created. Then, the patterns were detected by a model trained by Faster R-CNN net. Secondly, the approximate location of the pattern (the position of the whole patterns) were obtained based on the detected pattern. Thirdly, the precise positions of the pattern (geometric center points of pattern) were detected based on the approximate position results using the automatic threshold segmentation method. Missing center points were filled based on the four-neighbor-method to obtain a complete center point map. Finally, the skew angle and period length were measured based on the detected center points.

2.1. Image Acquisition and Pattern Dataset Creation

In this study, the image acquisition system was composed of a dome light source, a 1.3 megapixel color industrial camera, an LCD backlight and a servo motor module (see Figure 2). A vertically installed industrial camera with a camera lens overlooked the fabric. The dome light source that illuminated the fabric surface uniformly wasplaced in front of the fabric. In order to sample multiple parts of the piece, the system contained a servo mobile module that could move industrial cameras in a flat range. Figure 3 shows the six types of pattern images F_i, F_r, F_c, F_{s1}, F_{s2} and F_{s3} (the size was 1024×1280 pixels) acquired by the image acquisition system, where: F_i is the pattern with irregular shape. F_r is the pattern with circular shape. F_w is the pattern with the wavy shape. F_{s1}, F_{s2}, F_{s3} are patterns with a strip shape. The acquired images were transmitted to the data processing system (see

Figure 2) to be processed by the Faster R-CNN based algorithm. The image data processing is shown in Section 2.3.
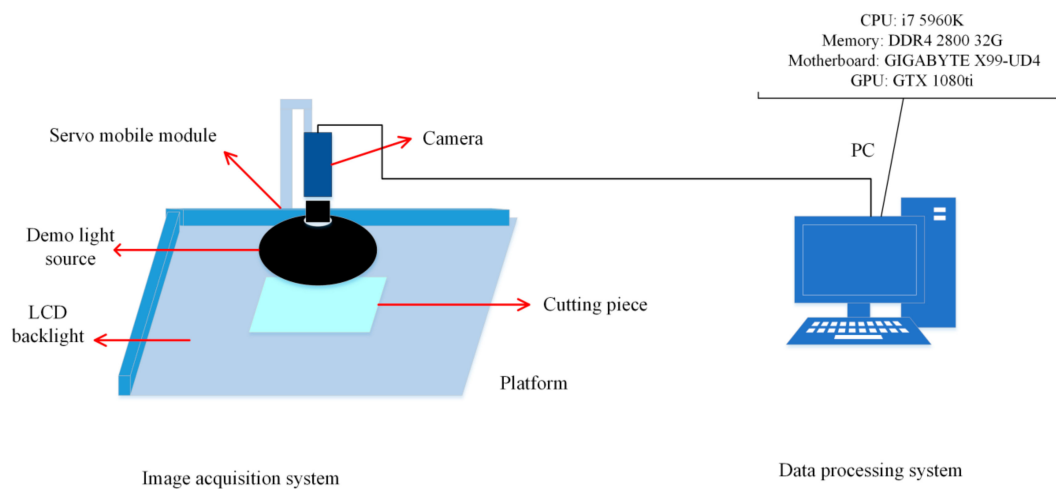
Figure 2. Image processing system. The image acquisition system on the left was used to acquire the partial texture image of the pattern, and the acquired images were three-channel RGB images and the size was 1024 × 1280 pixels. The acquired images were transmitted to the data processing system on the right for data processing.

(a) F_i	**(b)** F_r	**(c)** F_c
(d) F_{s1}	**(e)** F_{s2}	**(f)** F_{s3}
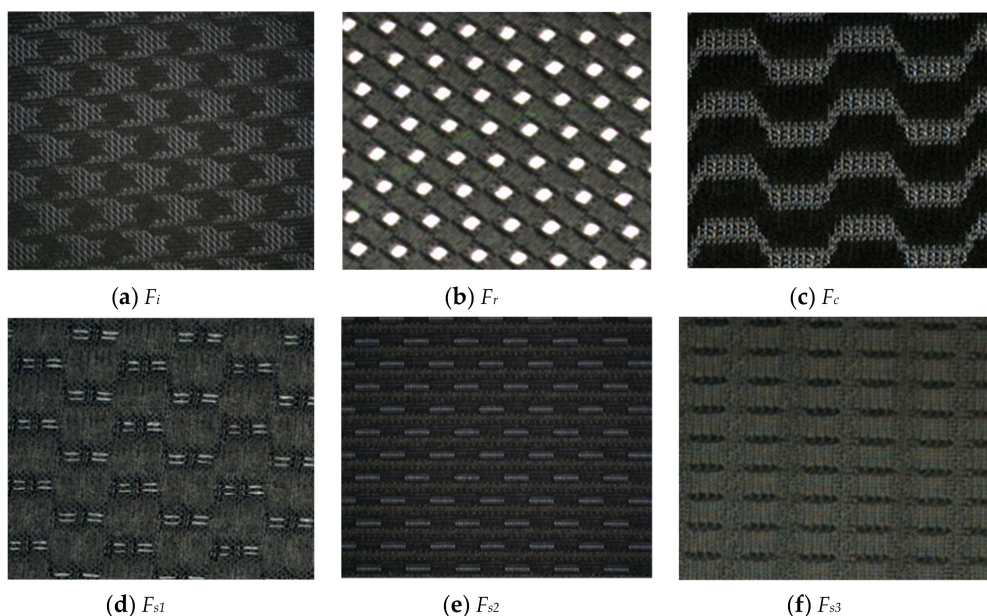
Figure 3. The sample images of different kinds of pattern piece. (**a**) irregular-shaped pattern F_i, (**b**) circular-shape pattern F_r, (**c**) wavy-shaped pattern F_c, (**d**) strip-shaped pattern F_{s1}, (**e**)strip-shaped pattern F_{s2}, (**f**) strip-shaped pattern F_{s3}.

In this paper, 5000 unique images with size of 640 × 512 × 3 pixels were contained in the pattern dataset, and each image contained approximately 20 to 50 patterns. These images were cropped from approximately 400 original images with size of 1280 × 1024 × 3 pixels. To obtain the best training effect, each image was labeled in detail. The key details for labeling each image were as follows:

- In order to avoid image over-fitting problems, each image contained 20–50 patterns, which were a critical metric for detection and recognition.
- The bounding box completely enclosed the pattern and kept the center coordinates of the pattern the same as the center coordinates of the bounding box.

- There are no overlapping regions between the bounding boxes and the dimensions of each bounding box remain the constant.

2.2. Training of Pattern Detection Model

In recent years, object detection technology has achieved rapid development, and the object detection network based on deep learning has greatly improved the ability of object detection. At present, there are two main methods: one depends on region proposal, such as R-CNN (region convolutional neural network) [17], Fast R-CNN [18], Faster R-CNN [13] and R-FCN [19]; the other does not rely on region proposal and directly estimates candidate object recommendations, such as SSD [20] and YOLO [21–23] family.

After R-CNN [17] and Fast R-CNN [18], Microsoft's Shaoqing Ren proposed Faster R-CNN [13] to optimize the running time of the detection network. The region proposal network (RPN) was proposed to generate the proposal region. RPN replaces the previous methods such as Selective Search [24] and EdgeBoxes [25] and it shares the convolution feature of the full map with the detection network so that the region proposal detection takes very little time. The Faster R-CNN structural framework consists of RPN + Fast R-CNN. The RPN network is mainly used to generate high-quality proposal region boxes, and Fast R-CNN is used to learn high-quality proposal region features and classify objects. The overall framework of Faster R-CNN is shown in Figure 4.

(**a**)

(**b**)
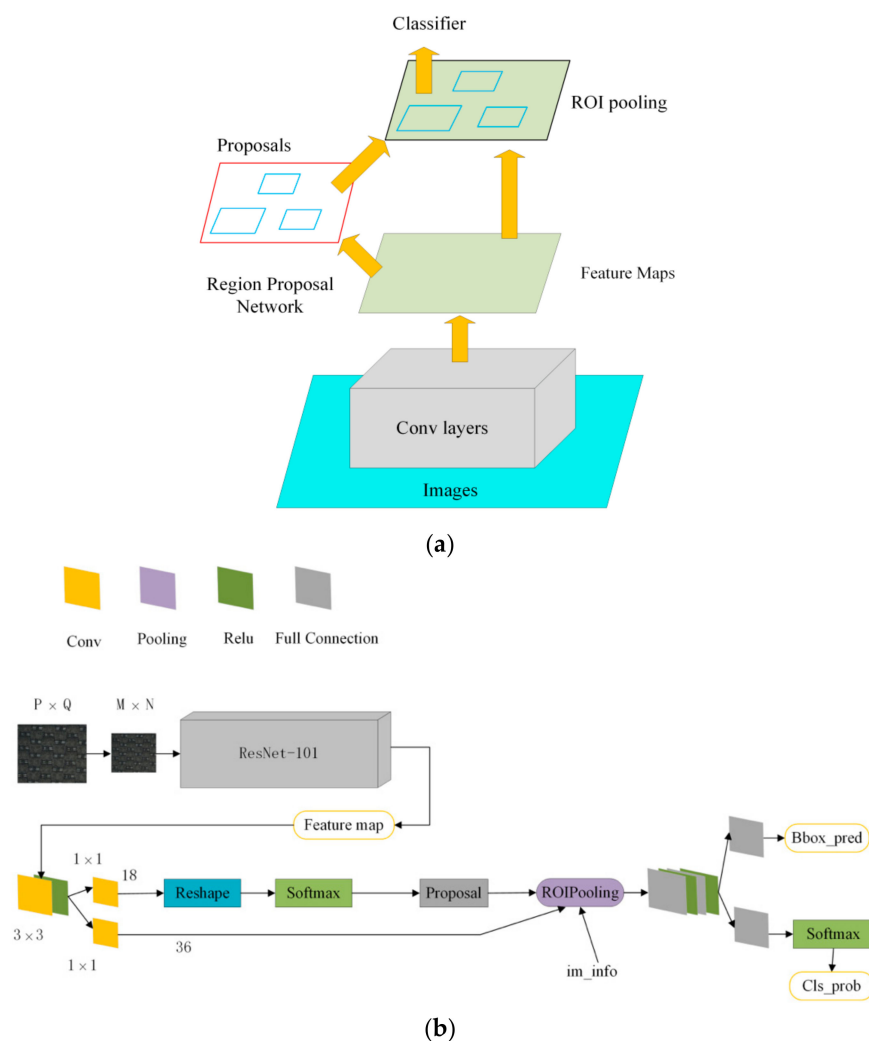
Figure 4. Faster region convolutional neural network (R-CNN) overall framework. (**a**) The streamlined flow chart of the Faster R-CNN framework [26]. (**b**) The detailed flow chart of the Faster R-CNN [13].

Faster R-CNN proposes the region proposal network and improves the efficiency of object detection. This provides feasibility for detecting multi-period patterns with Faster R-CNN. Three nets (ZF-Net [27], VGG16 [28] and Rse-Net-101 [29]) were respectively used as the pre-trained model of Faster R-CNN, where the pattern dataset contained 5382 patterns and a total of six types of patterns: F_i, F_r, F_w, F_{s1}, F_{s2} and F_{s3} (see Figure 3). The number of various pattern images was 894, 899, 902, 892, 904 and 891. Image size was 512×640 pixels. The pattern dataset was randomly divided into validation set, test set and train set according to the ratio of 2:2:6. Then, the divided datasets were used for training of Faster R-CNN (ZF-Net), Faster R-CNN (VGG16) and Faster R-CNN (ResNet-101), respectively. The experimental platforms included Windows 7, GPU GTX1080ti, Matlab 2014a and Visual Studio 2013, and the whole experiment was based on the deep learning framework Caffe.

The compared results are shown in Table 1, where the performance of the three pattern detection models can be seen. Precision represented the detection accuracy of the pattern. Balanced accuracy (Ba) was used to evaluate balanced accuracy of the pattern dataset. Kappa (K) was used to evaluate the accuracy of the pattern classification. Mean average precision (mAP) was the main indicator for evaluating the main detection results, because mAP was the actual metric for object detection.

Table 1. Evaluation of the Faster R-CNN with different pre-trained nets.

| Pre-Trained Net	Precision						K	Ba	mAP
	F_i	F_r	F_c	F_{s1}	F_{s2}	F_{s3}			
ZF	0.876	0.801	0.832	0.887	0.857	0.824	0.798	0.842	0.78
VGG16	0.879	0.864	0.864	0.904	0.886	0.857	0.824	0.884	0.81
ResNet-101	0.885	0.881	0.901	0.972	0.958	0.898	0.836	0.910	0.84

From Table 1, it can be concluded that the precision, K, Ba and mAP of the Resnet-101 net as the pre-trained model were higher than the other two nets, and thus Resnet-101 was chosen as the pre-trained model in this paper.

Figure 5 shows the detection results of the six patterns (F_i, F_r, F_w, F_{s1}, F_{s2} and F_{s3}) on the Faster R-CNN model. The boxes of different colors represent the different pattern categories detected by the model; the upper left corner of the box represents the classification result, pattern category and category score for the object of the box region. Since the patterns F_{s1}, F_{s2}, F_{s3} and F_r had the characteristics of large pattern pitch, small volume and regular shape, we chose to completely surround the pattern with the bounding box. The patterns F_i and F_c were irregular shapes and could not be completely surrounded by the bounding box, so we regarded a part of the pattern having the periodic characteristics as the detection object. It can be concluded from Figure 5 that the Faster R-CNN model could effectively detect six types of multi-period patterns and had fewer false positive and missing alarms.

Figure 6 shows the precision–recall (P–R) curve of the Faster R-CNN pattern detection model. The precision is the vertical axis, and the recall is the horizontal axis. The area value enclosed by the curve represents the mAP. It can be concluded from the Figure 6 that the pattern detection model had high accuracy, recall rate and average precision, so this model had pretty good pattern detection ability and excellent detection accuracy.
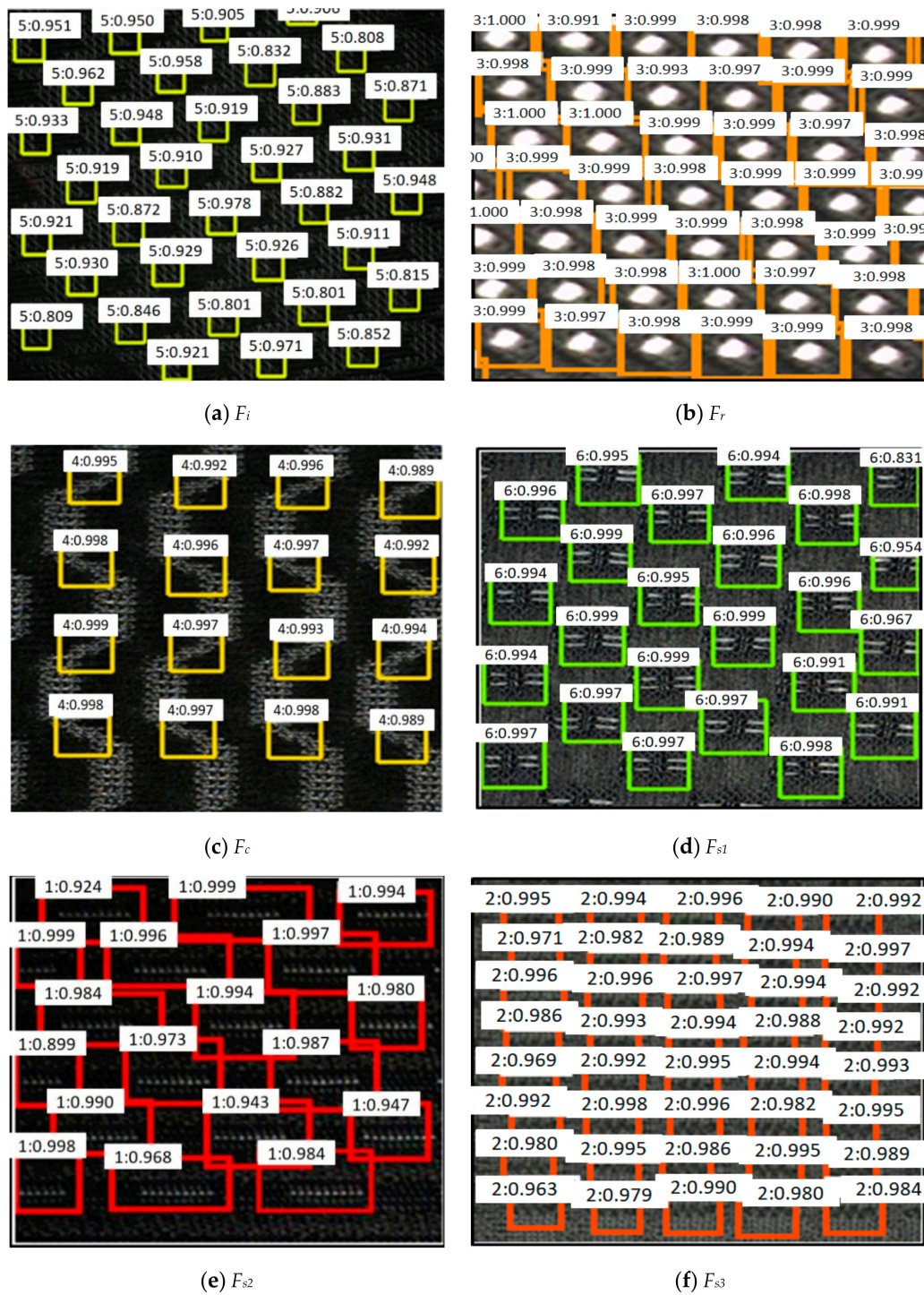
Figure 5. Detection results of the six types of patterns on the Faster R-CNN model. (**a**) Detection result of F_i. (**b**) Detection result of F_r. (**c**) Detection result of pattern F_c. (**d**) Detection result of F_{s1}. (**e**) Detection result of F_{s2}. (**f**) Detection result of F_{s3}.
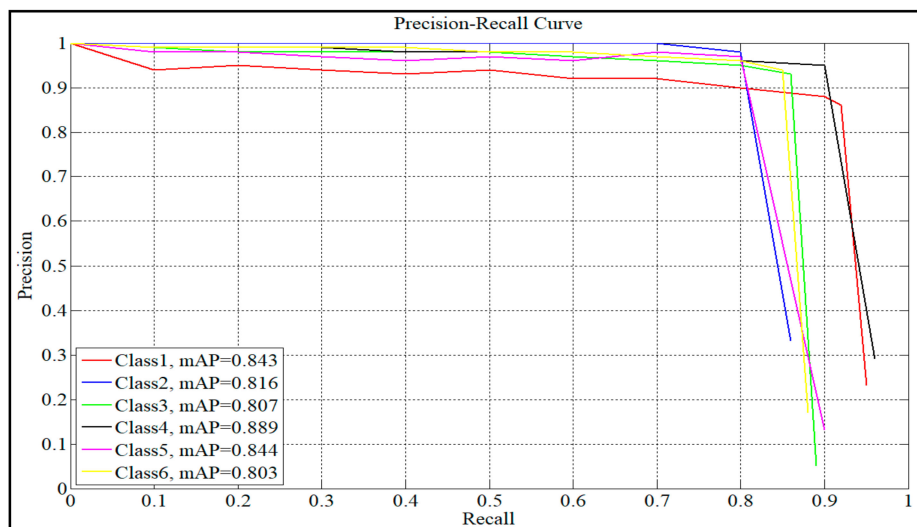
Figure 6. Precision–recall (P–R) curve of pattern detection by Faster R-CNN. The longitudinal axis indicates the detection precision, and the horizontal axis indicates the recall ratio. The area enclosed by the curve represents the mean average precision of the pattern detection.

2.3. Centre Point Extraction

The center point of the pattern is defined as the center of the region enclosed by the pattern outline. The area is defined as the number of pixels of a region. The center is calculated as the mean value of the line or column coordinates, respectively, of all pixels. The proposed method detected the approximate position of the pattern using the Faster R-CNN, and then an automatic threshold method was used to divide the pixel points of the pattern region and calculate the center coordinates. The steps are as follows:

Step 1: Image cropping method with overlapping areas is used for image cropping. The original image (Figure 7a) with size of 1208×1024 pixels is cropped into several sub-images (Figure 7b–e) of 640×512 pixels. The moving step length of the image cropping is approximately twice the length of the pattern period.

Step 2: The Faster R-CNN model is used to detect the pattern and output the classification score and categories. (Figure 7f–i).

Step 3: Merge sub-image F_{subi} according the coordinates of image cropping, obtaining image F_{new} (see Figure 8b). For example, define the coordinates of sub-image as (x_{sub}, y_{sub}), and the coordinates in image F_{new} as (x_{ori}, y_{ori}), so the coordinates (x_{ori}, y_{ori}) are computed as follows:

$$(x_{ori}, y_{ori}) = (x_{sub} + s_x \times (i-1), y_{sub} + s_y \times (j-1)) \tag{1}$$

where s_x and s_y are, respectively, the horizontal moving step length and the longitudinal moving step length. The variables i ($i = 1, 2, 3 \dots$) and j ($j = 1, 2, 3 \dots$), respectively, represent the times of horizontal and vertical cropping. Then combine the overlapping bounding boxes into one large bounding box according the maximum coordinates of overlapping bounding boxes, getting image F_{new1} (see Figure 8c).

Step 4: Correct the inaccurate bounding boxes and calculate the center points of the patterns to get the original center point map. First, the grey distribution information of the original image is counted by the grey histogram and the average grey value G_{th} is calculated. Second, G_{th} is used as a threshold to segment the patterns in the bounding boxes and calculate the area S_i ($i = 1, 2 \dots$) of segmented pattern, the average value S_{av} of S_i, the center point P_p of the pattern, and the center point P_b of the bounding box. Third, compare the size of S_i and S_{av}, and remove the bounding boxes which $S \le S_{av}$. Fourth, adjust the positions of bounding boxes by moving the bounding boxes toward P_p to make $S > S_{av}$. Finally, segment the patterns f in the corrected bounding boxes using the threshold

segmentation method and calculate them center points to obtain the original center point map (see Figure 9a).

$$f(x,y) = \begin{cases} 1 & f(x,y) > G_{th} \\ 0 & f(x,y) \le G_{th} \end{cases}. \tag{2}$$

Step 5: Missing center points are filled based on four-neighbor-method to obtain the final center point map (see Figure 9c). First, approximately weft period length T_{hx} and approximately warp period length T_{hy} are counted from the original center point map. Second, the missing center point is between two known adjacent points A and B. If $(k + 1/2) < T_{hx} < d_m < (k + 3/2) T_{hx}$, where $k = 1, 2 \ldots$, and d_m is the distance between two adjacent corners A and B, then fill in k missing center points uniformly on the line AB. Suppose the filled point is N. Third, find two adjacent points C and D of N in the longitudinal direction. Finally, the missing point M (see Figure 9b) is the intersection between L_1 (the line formed by point A and point B) and L_2 (the line formed by point C and point D). Similarly, handle the cases with missing points in the vertical direction.
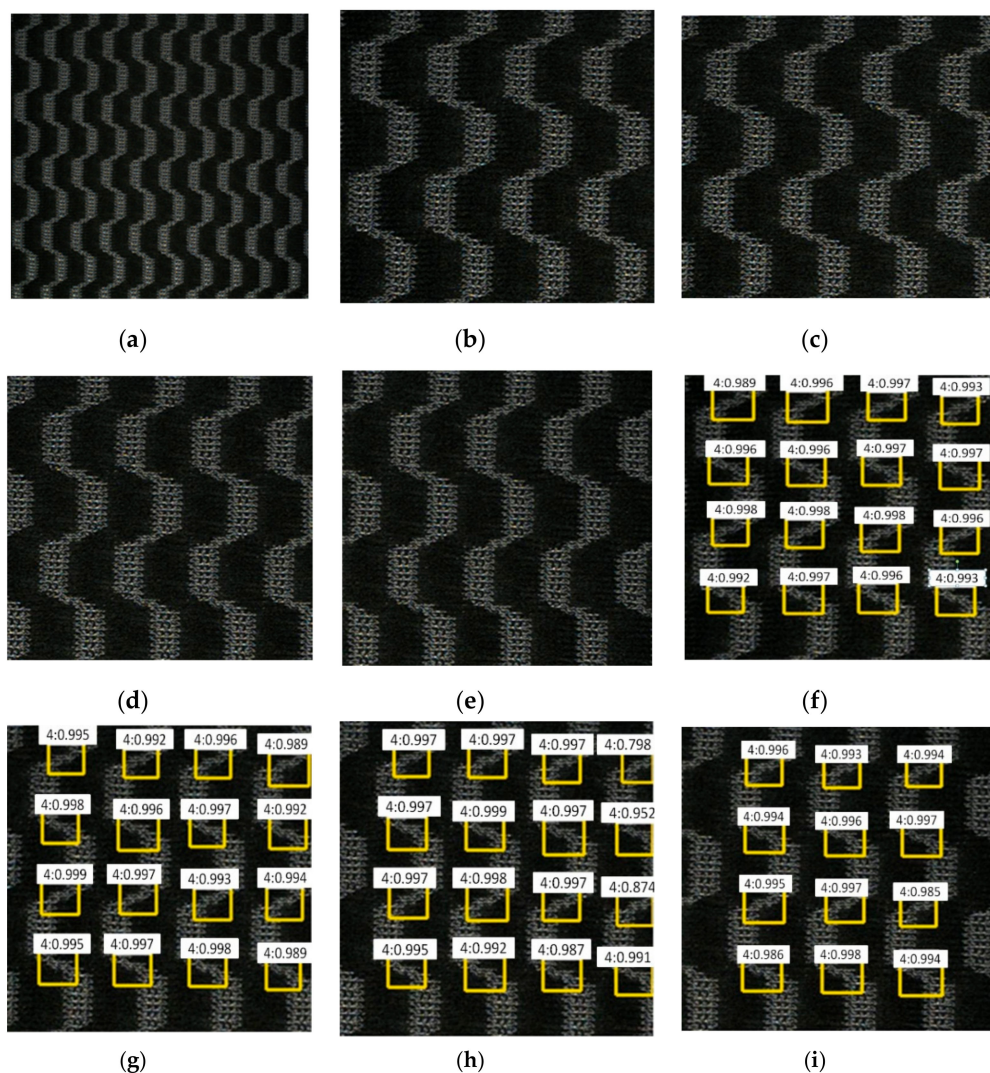
Figure 7. Intermediate process of the proposed method. (**a**) Original image. (**b**) Sub-image F_{sub1}. (**c**) Sub-image F_{sub2}. (**d**) Sub-image F_{sub3}. (**e**) Sub-image F_{sub4}. (**f**) Detection results of F_{sub1}. (**g**) Detection results of F_{sub2}. (**h**) Detection results of F_{sub3}. (**i**) Detection results of F_{sub4}.
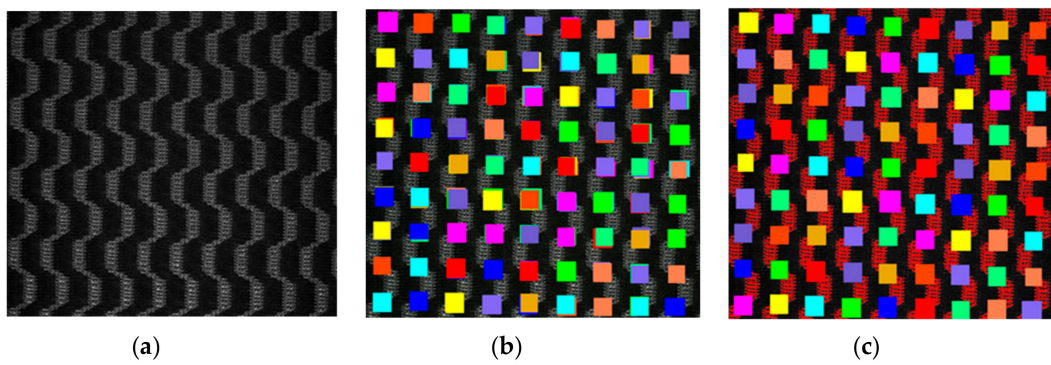
Figure 8. Bounding box mapping process. (**a**) Original image. (**b**) Bounding box mapping result F_{new}. (**c**) Bounding box merge result F_{new1}.
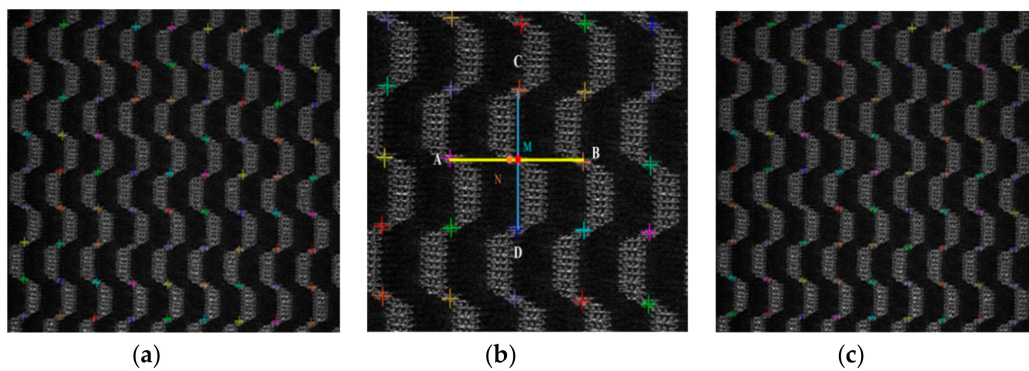

Figure 9. The procedure of the proposed method. (**a**) Original center point map. (**b**) Missing point filling process. (**c**) Final center point map.

2.4. Pattern Period Length and Skew Angle Measurement

The skew angles and period length can be measured based on the final center point map which reflects the center points distribution of the pattern.

The period lengths include the weft period length T_h and warp period length T_v. As shown in Figure 10b, the detected center points were denoted by the red points H_i, V_i, $(i = 1, 2, 3, \dots)$. One weft period length is $T_h = d_{HiHj}$, where d_{HiHj} is the distance between the H_i and H_j $(j = i + 1, i = 1, 2, 3 \dots)$. Similarly, one warp period length is $T_v = d_{ViVj}$, where d_{ViVj} is the distance between the V_i and V_j $(j = i + 1, i = 1, 2, 3 \dots)$.
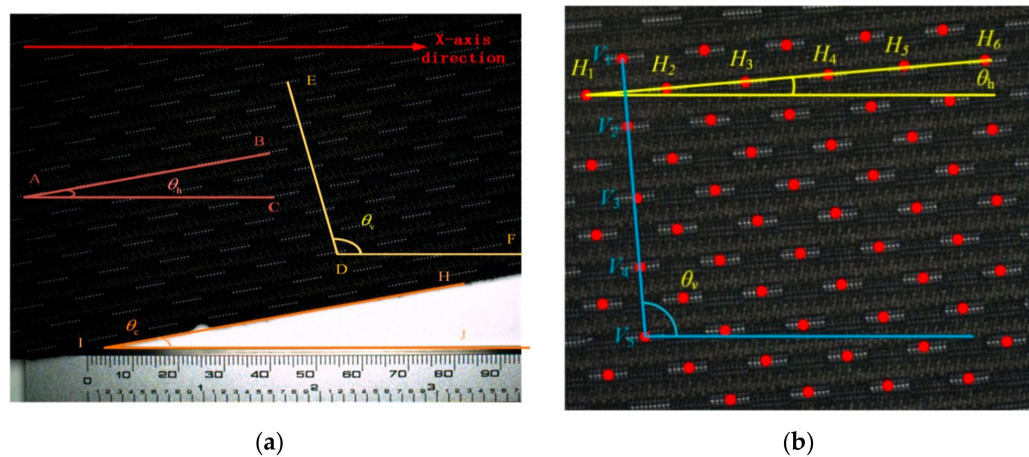
Figure 10. Measurement of the skew angles and period length. (**a**) Schematic diagram of pattern parameter measurement. (**b**) The pattern center points map of (**a**).

The skew angles also include the weft skew angle θ_{weft} and warp skew angle θ_{warp}. The θ_{weft} and θ_{warp} are calculated by θ_h, θ_v and θ_c in Figure 10a, where θ_c is the angle between the contour of the piece and the x-axis, measured by the measuring tool (see Figure 10a). Since this paper only studied the local pattern features of the piece, it is assumed that θ_c is a known angle. The way to obtain θ_h and θ_v is shown in Figure 10b. First, the least squares method is used to fit the center points H_i ($i = 1, 2, 3 \ldots$) in the weft direction as a weft period line L_h. Second, calculate the slope K_h of the line L_h. Finally, θ_h is calculated by the equation $\theta = \arctan(k)$. Similarly, the center points V_i ($i = 1, 2, 3 \ldots$) in the weft direction are used to obtain θ_v. The skew angles (θ_{weft} and θ_{warp}) can be obtained by the following equation:

$$(\theta_{wef}, \theta_{warp}) = (\theta_h - \theta_c, \theta_v - \theta_c) \tag{3}$$

3. Results and Discussion

In this section, the proposed algorithm was used to test the six types of pattern images (F_i, F_r, F_c, F_{s1}, F_{s2} and F_{s3}) shown in Figure 11a–f. The center point maps reflecting the periodic characteristics of the pattern are shown in Figure 11g–l. Since θ_c in Figure 10a is an external angle and does not affect the overall accuracy of the angle to be measured, this paper measured and evaluated the θ_h and θ_v shown in Figure 10a.

To evaluate the proposed algorithm, we compare the proposed algorithm with manual measurement results. Manual measurement of the period length was achieved by clicking the center points of the patterns on the computer screen. As illustrated in Figure 12b, for example, we obtained the center points H_i, V_i, ($i = 1, 2, \ldots$) and then calculated the weft period length as $T_h = d_{HiHj}$, where d_{HiHj} is the distance between the H_i and H_j ($j = i + 1, i = 1, 2, \ldots$).And the warp period length as $T_v = d_{ViVj}$, where d_{ViVj} is the distance between the V_i and V_j ($j = i + 1, i = 1, 2, \ldots$). T_h and T_v were measured twenty times, and the final result was the average of the measurements. Similarly, manual measurement of the θ_h and θ_v also was accomplished by clicking the center points of the patterns on the computer screen. The center points in the same period direction were fitted as a straight line and the angle between the line and the x-axis was calculated (see Figure 11a). We measured each angle twenty times and then calculated the average values to obtain the result. The standard deviation δ was used to analyze the accuracy of the manual measurements of the period length and skew angle.

(**a**) F_{s2}　　　　　　　　　(**b**) F_r　　　　　　　　　(**c**) F_{s3}

(**d**) F_{s1}　　　　　　　　　(**e**) F_c　　　　　　　　　(**f**) F_i

(**g**) Centre point map of F_{s2}　　　(**h**) Centre point map of F_r　　　(**i**) Centre point map of F_{s3}

(**j**) Centre point map of F_{s1}　　　(**k**) Centre point map of F_c　　　(**l**) Centre point map of F_i
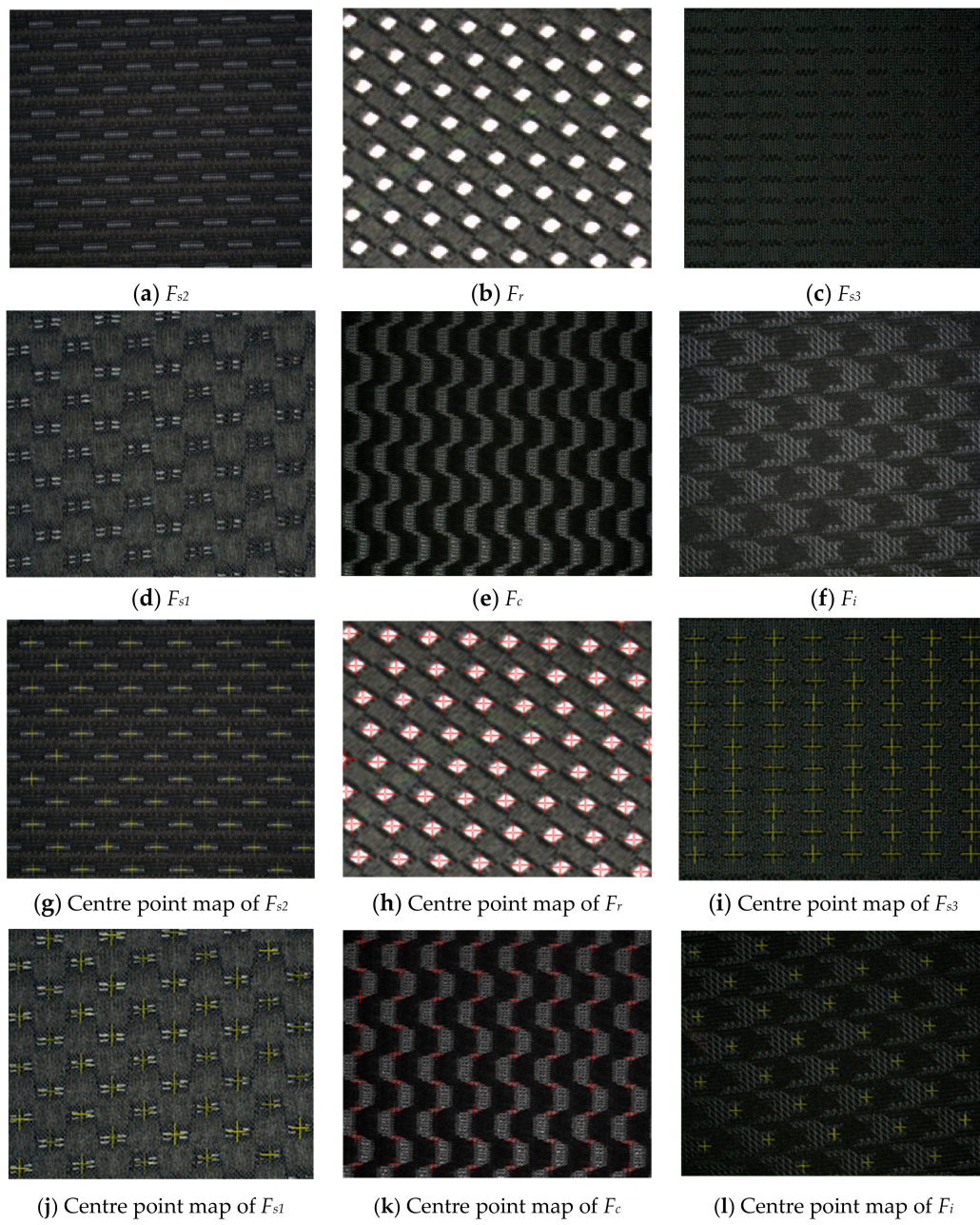
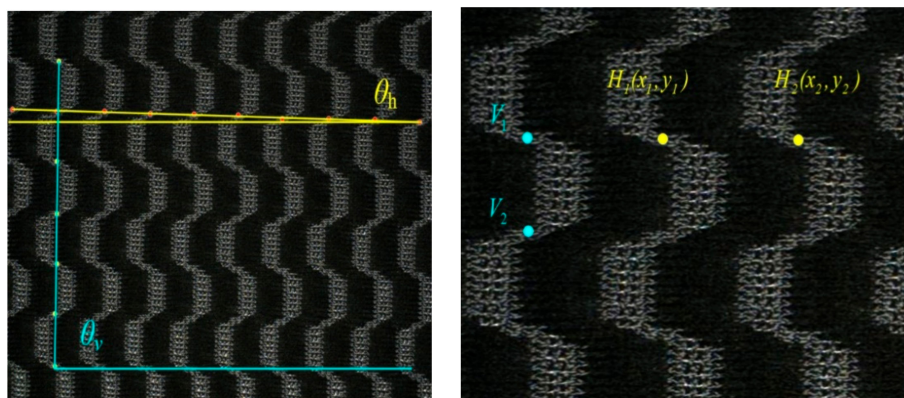**Figure 11.** Six types of pattern images and their center point maps.

Figure 12. Manual measurement of parameters. (**a**) Skew angle, (**b**) period length.

The expression of the standard deviation is shown as follows:

$$\delta = \sqrt{\frac{1}{N}\sum_{i=1}^{N}\left(X_i - \bar{X}\right)^2} \tag{4}$$

where $\bar{X}$ is the average value of X.

Table 2 shows the manual measurement standard deviation of period length of images (F_r, F_c, F_{s1}, F_{s2} and F_{s3}), where $\delta_{Th\alpha}$, $\delta_{Th\beta}$, and $\delta_{Th\gamma}$ were the minimum, maximum and average standard deviation, respectively, of the weft period length measurement. $\delta_{Tv\alpha}$, $\delta_{Tv\beta}$, and $\delta_{Tv\gamma}$ were defined similarly for the warp period length measurement. As shown in Table 2, the standard deviation obtained by manual measurement was very small. Therefore, it was reasonable to use the manual measurement results as the evaluation standard.

Table 2. Standard deviation of manual measurement of period length.

Image	Standard Deviation of T_h			Standard Deviation of T_v		
	$\delta_{Th\alpha}$	$\delta_{Th\beta}$	$\delta_{Th\gamma}$	$\delta_{Tv\alpha}$	$\delta_{Tv\beta}$	$\delta_{Tv\gamma}$
F_{s2}	0.044	0.378	0.081	0.006	0.286	0.175
F_r	0.069	0.451	0.167	None	None	None
F_{s3}	0.018	0.237	0.146	0.046	0.588	0.392
F_{s1}	0.008	0.164	0.132	0.052	0.682	0.458
F_c	0.157	0.533	0.259	0.098	0.226	0.181
F_i	0.088	0.576	0.472	0.038	0.574	0.282

Table 3 shows the period length measurement results of images (F_i, F_r, F_c, F_{s1}, F_{s2} and F_{s3} in Figure 11). The method based on image autocorrelation, the method based on distance matching function and the proposed method were compared with the manual measurement results, where T is the period length, the subscript h represents the weft direction, the subscript v represents the warp direction, m stands for manual measurement method, p stands for the proposed method, z stands for autocorrelation, d stands for distance matching function.

Table 3. Period length measurement results of various methods.

Image	T_{hm}	T_{hp}	T_{hz}	T_{hd}	T_{vm}	T_{vp}	T_{vz}	T_{vd}
F_{s2}	204.8	203.6	208.3	206.4	178.6	177.3	180.1	176.6
F_r	90.2	90.1	93.4	95.8	None	None	None	None
F_{s3}	102.2	101.8	202.8	128.5	62.8	63.7	59.7	65.4
F_{s1}	176.0	177.2	58.7	168.2	120.6	120.8	119.0	121.5
F_c	125.7	125.4	128.8	130.7	114.8	114.2	130.0	120.1
F_i	271.4	270.3	243.5	256.2	269.8	267.2	273.5	264.6

Table 4 shows the relative error value between different period length measurement methods and manual measurements of images (F_i, F_r, F_c, F_{s1}, F_{s2} and F_{s3} in Figure 11), where the e_{hpm} represents the relative error of T_{hp} with T_{hm}. e_{hzm} represents the relative error of T_{hz} with T_{hm}. e_{hdm} represents the relative error of T_{hd} with T_{hm}. Similarly, e_{vpm} is the relative error of T_{vp} with T_{vm}. e_{vzm} is the relative error of T_{vz} with T_{vm}. e_{vdm} is the relative error of T_{vd} with T_{vm}. The expression of the relative error RE is shown in the following Equation (5).

$$RE = \frac{X - T}{T} \times 100\% \tag{5}$$

where X represents the measured value and T represents the actual value.

Table 4. Relative errors of the period length measurements for the multi-period pattern piece.

Image	e_{hpm} (%)	e_{hzm} (%)	e_{hdm} (%)	e_{vpm} (%)	e_{vzm} (%)	e_{vdm} (%)
F_{s2}	0.587	1.709	0.781	0.728	0.839	1.119
F_r	0.111	3.548	6.208	None	None	None
F_{s3}	0.391	98.434	25.734	1.433	4.936	4.140
F_{s1}	0.682	66.647	4.432	0.166	1.326	0.746
F_c	0.239	2.466	3.978	0.523	13.240	4.617
F_i	0.405	10.280	5.601	0.964	1.371	1.927

From Tables 3 and 4, we could conclude that the period length measured by the proposed method had higher accuracy than the autocorrelation-based and the distance-matching function-based method. There was also a smaller relative error between the proposed method and the manual measurement result.

Similar to the evaluation of the period length, the standard deviation was used to suggest the reliability of the manual measurement of the angles. Table 5 shows the manual measurement standard deviation of θ_h and θ_v of images (F_i, F_r, F_c, F_{s1}, F_{s2} and F_{s3} in Figure 11), where the $\delta_{\theta h \alpha}$, $\delta_{\theta h \beta}$ and $\delta_{\theta h \gamma}$ are the minimum, maximum and average standard deviation of the θ_h, respectively. Similarly, $\delta_{\theta v \alpha}$, $\delta_{\theta v \beta}$ and $\delta_{\theta v \gamma}$ are the minimum, maximum and average standard deviation of the θ_v, respectively. From Table 5, we could conclude that the standard deviation of the manual measurements was small. Therefore, it was reasonable to use the manual measurement results as a benchmark to evaluate the measurement accuracy of the proposed measurement method.

Table 5. Standard deviation of manual measurement of θ_h and θ_v.

Image	Standard Deviation of θ_h			Standard Deviation of θ_v		
	$\delta_{\theta h \alpha}$	$\delta_{\theta h \beta}$	$\delta_{\theta h \gamma}$	$\delta_{\theta v \alpha}$	$\delta_{\theta v \beta}$	$\delta_{\theta v \gamma}$
F_{s2}	0.032	0.221	0.076	0.007	0.274	0.129
F_r	0.093	0.727	0.364	None	None	None
F_{s3}	0.009	0.158	0.074	0.171	0.447	0.300
F_{s1}	0.003	0.077	0.052	0.061	0.115	0.079
F_c	0.067	0.082	0.022	0.009	0.238	0.166
F_i	0.025	0.094	0.037	0.018	0.049	0.026

Table 6 shows the various methods measurement results of θ_h and θ_v of images (F_i, F_r, F_c, F_{s1}, F_{s2} and F_{s3} in Figure 11). The method based on corner detection method and the proposed method for measuring θ_h and θ_v were compared with the manual measurement results, where the subscript h represents the weft direction, the subscript v represents the warp direction, m stands for manual measurement method, p stands for the proposed method, c stands for corner detection.

Table 6. Measurement results of various methods of θ_h and θ_v.

Image	θ_{hm} (°)	θ_{vm} (°)	θ_{hp} (°)	θ_{vp} (°)	θ_{hc} (°)	θ_{vc} (°)
F_{s2}	0.182	88.502	0.188	88.424	0.397	84.186
F_r	3.578	None	3.686	None	4.858	None
F_{s3}	1.552	88.105	1.534	87.845	2.434	82.428
F_{s1}	1.784	86.238	1.779	86.173	2.379	89.327
F_c	1.874	88.386	1.824	88.693	1.467	85.486
F_i	2.836	86.332	2.868	86.546	3.542	88.248

Table 7 shows the relative error value between different angle measurement methods and manual measurements of images (F_i, F_r, F_c, F_{s1}, F_{s2} and F_{s3} in Figure 11), where the e_{hpm} represents the relative error of θ_{hp} with θ_{hm}. e_{vpm} represents the relative error of θ_{vp} with θ_{vm}. e_{hcm} represents the relative error of θ_{hc} with θ_{hm}. e_{vcm} represents the relative error of θ_{vc} with θ_{vm}.

Table 7. Relative errors of the angle measurements for the multi-period pattern piece.

Image	e_{hpm} (%)	e_{vpm} (%)	e_{hcm} (%)	e_{vcm} (%)
F_{s2}	3.297	0.088	118.131	4.877
F_r	3.018	None	35.434	None
F_{s3}	1.159	0.295	56.829	6.443
F_{s1}	0.280	0.075	98.991	3.582
F_c	2.668	0.347	21.238	3.281
F_i	1.128	0.248	24.894	2.219

The following observations were derived from Tables 6 and 7. The proposed method for measuring θ_h and θ_v achieved a smaller relative error compared to manual measurements. Compared with the corner detection-based method, the proposed method had higher accuracy and more stable performance in angle measurement.

4. Conclusions

The measurement of the skew angle and the period length is a fundamental problem in the quality inspection of multi-period pattern cutting pieces. We demonstrated a solution that Faster R-CNN efficiently detected the approximate location of the pattern and the method based on threshold achieved the precise location of pattern, which achieved the measurement of the skew angle and period length with high accuracy. We believe this work opens up exciting research opportunities to use the object detection network to extract the fabric pattern period, providing a new way to study pattern periodicity and can improve the detection accuracy of the pattern parameters.

References

1. Reber, J.K.; Jill, A.R. Method and Apparatus for Cutting Pieces of Cloth for Use in Quilts or the Like. U.S. Patent No. 5,557,996, 24 September 1996.
2. Miao, Y.E. Image texture detection based on parallel gray level grade co-occurrence matrix. *Laser Infrared* **2011**, *41*, 1287–1291.
3. Sheng, J.; Guo-An, T.; Yang, T. Automatic Extraction Method for Texture Periodicity Based on Improved Normalized Distance Matching Function. *Pattern Recognit. Artif. Intell.* **2014**, *27*, 1098–1104.
4. Rocio, L.M.; Raul, E.; Sanchez, Y.; Victor, A.R. Periodicity and Texel Size Estimation of Visual Texture Using Entropy Cues. *Comput. Sist.* **2010**, *14*, 309–319.
5. Li, J.; Yang, Y.Q.; Shen, W.; Li, D.; Zhou, H. Research on fabric texture based on gray level co-occurrence matrix. *Adv. Text. Technol.* **2013**, *3*, 12–16.
6. Xiao, Z.; Nie, X.; Zhang, F.; Geng, L. Recognition for woven fabric pattern based on gradient histogram. *J. Text. Inst.* **2014**, *105*, 744–752. [CrossRef]
7. Jing, J.F.; Yang, P.P.; Li, P.F. Determination on design cycle of printed fabrics based on distance matching function. *J. Text. Res.* **2015**, *36*, 98–103.
8. Jian, Z.; Jingan, W.; Ruru, P.; Weidong, G. Periodicity Measurement for Fabric Texture by Using Frequency Domain Analysis and Distance Matching Function. *J. Donghua Univ.* **2017**, *43*, 629–633.
9. Ning, W.U.; Shengqi, G.; Shuaihua, X.U. Fabric Defect Detection Based on Periodicity and Local Directivity of Texture Edge. *Comput. Mod.* **2014**, *4*, 16–19.
10. Kahaki, S.; Nordin, M.; Ashtari, A. Contour-based corner detection and classification by using mean projection transform. *Sensors* **2014**, *14*, 4126–4143. [CrossRef] [PubMed]

11. Xiao, Z.; Pei, L.; Zhang, F.; Lei, G.; Wu, J.; Tong, J.; Xi, J.T.; Ogunbona, P. Measurement of surface parameters of three-dimensional braided composite preform based on curvature scale space corner detector. *Text. Res. J.* **2018**, *88*, 2641–2653. [CrossRef]

12. Xiao, Z.; Pei, L.; Zhang, F.; Sun, Y.; Geng, L.; Wu, J.; Tong, J.; Wen, J. Surface parameters measurement of braided preform based on local edge extreme. *J. Text. Inst.* **2019**, *110*, 535–542. [CrossRef]

13. Ren, S.; He, K.; Girshick, R.; Sun, J. Faster r-cnn: Towards real-time object detection with region proposal networks. *IEEE Trans. Pattern Anal. Mach. Intell.* **2015**, *39*, 91–99. [CrossRef] [PubMed]

14. Xu, Z.; Yang, W.; Meng, A.; Lu, N.; Huang, H.; Ying, C.; Huang, L. Towards End-to-End License Plate Detection and Recognition: A Large Dataset and Baseline. In Proceedings of the European Conference on Computer Vision (ECCV), Munich, Germany, 8–14 September 2018; pp. 255–271.

15. Tian, Z.; Huang, W.; He, T. Detecting text in natural image with connectionist text proposal network. In Proceedings of the European Conference on Computer Vision, Amsterdam, The Netherlands, 11–14 October 2016; pp. 56–72.

16. Ren, Y.; Zhu, C.; Xiao, S. Small object detection in optical remote sensing images via modified faster R-CNN. *Appl. Sci.* **2018**, *8*, 813. [CrossRef]

17. Girshick, R.; Donahue, J.; Darrell, T.; Malik, J. Rich feature hierarchies for accurate object detection and semantic segmentation. In Proceedings of the IEEE Conference on Computer Vision and Pattern Recognition, Columbus, OH, USA, 23–28 June 2014; pp. 580–587.

18. Girshick, R. Fast r-cnn. In Proceedings of the IEEE International Conference on Computer Vision, Santiago, Chile, 11–18 December 2015; pp. 1440–1448.

19. Dai, J.; Li, Y.; He, K.; Sun, J. R-fcn: Object detection via region-based fully convolutional networks. In Proceedings of the 30th International Conference on Neural Information Processing Systems, Barcelona, Spain, 5–10 December 2016; pp. 379–387.

20. Liu, W.; Anguelov, D.; Erhan, D.; Szegedy, C.; Reed, S.; Fu, C.; Berg, A.C. SSD: Single Shot MultiBox Detector. In Proceedings of the European Conference on Computer Vision, Amsterdam, The Netherlands, 11–14 October 2016; pp. 21–37.

21. Joseph, R.; Santosh, D.; Ross, G.; Ali, F. You only look once: Unified, real-time object detection. In Proceedings of the IEEE Conference on Computer Vision and Pattern Recognition, Las Vegas, NV, USA, 27–30 June 2016; pp. 779–788.

22. Yang, W.; Zhang, Z.; Wang, H.; Zhang, J. A vehicle real-time detection algorithm based on YOLOv2 framework. In Proceedings of the Real-Time Image and Video Processing 2018, Orlando, FL, USA, 15–19 April 2018.

23. Redmon, J.; Ali, F. Yolov3: An incremental improvement. *arXiv* **2018**, arXiv:1804.02767.

24. Uijlings, J.R.; Van De Sande, K.E.; Gevers, T.; Smeulders, A.W. Selective search for object recognition. *Int. J. Comput. Vis.* **2013**, *104*, 154–171. [CrossRef]

25. Lawrence Zitnick, C.; Piotr, D. Edge boxes: Locating object proposals from edges. In Proceedings of the European Conference on Computer Vision, Zurich, Switzerland, 6–12 September 2014; pp. 391–405.

26. R-CNN, Fast R-CNN, Faster R-CNN, YOLO—Comparisions. Available online: https://towardsdatascience.com/r-cnn-fast-rcnn-faster-r-cnn-yolo-object-detection-algorithms-36d53571365e (accessed on 10 February 2019).

27. Zeiler, M.D.; Rob, F. Visualizing and understanding convolutional networks. In Proceedings of the European Conference on Computer Vision, Zurich, Switzerland, 6–12 September 2014; pp. 818–833.

28. Simonyan, K.; Zisserman, A. Very deep convolutional networks for large-scale image recognition. *arXiv* **2014**, arXiv:1409.1556.

29. He, K.; Zhang, X.; Ren, S.; Sun, J. Deep residual learning for image recognition. In Proceedings of the IEEE Conference on Computer Vision and Pattern Recognition, Las Vegas, NV, USA, 26 June–1 July 2016; pp. 770–778.